***An experimental study into the ultimate capacity of an "impression" pile in clay***

**Authors:**

Leonardo Maria Lalicata, MSc, PhD*

Sarah Elizabeth Stallebrass, MA, PhD*

Andrew McNamara, MSc, PhD*

* City, University of London, London, England, United Kingdom, EC1V 0HB

**Corresponding author:**

Dr Leonardo Maria Lalicata

leonardo.lalicata@city.ac.uk

***Abstract***

The ultimate capacity of a novel type of piled foundation called an "impression" pile has been investigated using centrifuge modelling techniques. The name derives from the small discrete impressions created in the side walls of a bored cast in situ pile to increase the soil/pile friction such that the impressions form nodules on the shaft of the concreted pile. The technology is suitable for bored piles in overconsolidated clay, such as London Clay. The experiments explored the influence of geometrical parameters such as the vertical spacing of the impressions, their number at each level and their shape. The data show a consistent increase in pile capacity of 40% when the impressions extend over 85% of the pile length. The ultimate capacity of the pile is primarily affected by the length of the pile which is impressed, the number of nodules at a given cross section and the spacing of the nodules in the vertical direction, as long as this is greater than a threshold value. According to the experimental evidence, a block failure occurs for a spacing lower than this threshold value. Plastic failure mechanisms for the impression pile were established. These were used successfully to calculate the ultimate capacity of the impression piles tested with an error of less than 10%.

*Keywords:* impression pile, centrifuge modelling, axial loading, overconsolidated clay, enhanced capacity

**List of notations**

| | |
|---|---|
| $A$ | cross section of the pile |
| $A_{nod}$ | cross section of the nodule |
| $b$ | protruded length of the nodule (or rib) |
| $CL$ | centre line |
| $CSL$ | critical state line |
| $d$ | pile diameter |
| $G_s$ | Specific gravity |
| $g$ | gravity acceleration |
| $h$ | height of the nodule (or rib) |
| $L$ | pile length |
| $l$ | width of the nodule (or rib) |
| $L_a$ | active length of the impression pile |
| $n$ | number of nodules in the cross section of the pile |
| $M$ | Slope of the critical state line in the q-p’ plane |
| $N_c$ | end bearing factor for the undrained shear strength |
| $N_{c,nod}$ | nodule end bearing factor for the undrained shear strength |
| $N_{c,PL}$ | rib end bearing factor for the undrained shear strength under plain strain condition |
| $N_{c,rib}$ | rib end bearing factor for the undrained shear strength |
| $OCR$ | overconsolidation ratio |
| $p'$ | mean effective stress |
| $P_{ext}$ | circumference of the pile plus rib |
| $P_{pile}$ | circumference of the pile |
| $Q$, $Q_u$ | load on the pile, capacity of the pile |
| $Q_b$ | base capacity |
| $q_b$ | bearing pressure |
| $Q_{b,nod}$ | base capacity the nodule |
| $Q_s$ | shaft capacity |
| $Q_{s,block}$ | shaft capacity between two connecting ribs |
| $Q_{s,in\ La}$ | shaft capacity inside the active length |

$Q_{s,intra\ nod}$ shaft capacity between the vertical blocks connecting the nodules

$Q_{s,nod}$ shaft capacity on the vertical blocks connecting the nodules

$Q_{s,out\ La}$ shaft capacity outside the active length

$Q_{s,single}$ shaft capacity on two individual ribs

$s$ vertical spacing between two horizons of nodules (or ribs)

$s_u$, $s_{u,w}$, $s_{u,vane}$, $s_{u\ (base)}$ undrained shear strength, undrained shear strength from water content, undrained shear strength from hand vane test, undrained shear strength at the pile base

$v$ specific volume

$W$ dead weight of the pile

$w$ gravimetric water content

$z$ depth

$\Gamma$ specific volume on the CSL at $p'$=1 kPa

$\alpha$ soil-pile adhesion factor

$\delta$ pile head settlement

$\gamma$ unit weight of soil

$\lambda$ slope of the normal compression line in the $v$-$lnp'$ space

$\sigma_v$ vertical stress

$\xi$ shape factor

***Introduction***

Very often, the most important factor in determining the ultimate capacity of a pile subjected to axial load is the shaft resistance. In clays, the maximum shear stress developed on the pile shaft is often assumed to be a fraction of the undrained shear strength of the soil, $s_u$. The adhesion factor, $\alpha$, is an empirical parameter that defines this fraction and accounts for the disturbance created during the construction of the pile. It depends on the process used in constructing the pile, the properties of the clay and the site conditions (such as relative humidity and drainage towards the pile bore). For piles embedded in stiff clays $\alpha$ can be as low as 0.35 or 0.5, depending on the construction technology used (Cherubini and Vessia, 2007). It is attractive therefore to develop a new construction technique that aims to improve the soil-pile interface strength.

Over the years, many piling contractors have experimented with various methods for enhancing shaft capacity (Hard and Carvalho, 2018; Karkee *et al.*, 1988; Watanabe et al., 2011; Zhou *et al.*, 2020; Stainer *et al.*, 2011); including the manufacture of special tools to scrape concentric rings that protrude beyond the nominal pile diameter (Ground Engineering, 2003; Hard and Carvalho, 2018). This produces a ribbed profile along the shaft which has the effect, in an ultimate capacity test, of creating a failure surface between the ribs where there is a soil-soil interface. However, owing to the obvious commercial benefits that might accrue from such a development, there is very little published material relating to pile shaft modification. Ground Engineering (2003) described some field trials on ribbed piles. The ribs were found to enhance the ultimate capacity of 750mm diameter piles, constructed in glacial clay, by as much as 30%. Gorasia and McNamara (2016) presented the results of a series of centrifuge tests on ribbed piles demonstrating that the capacity increase could reach 40% for a pile 800mm in diameter with ribs protruding by 75mm (at prototype scale). Small scale tests by Qian *et al.* (2016) demonstrated that the pull-out capacity of a ribbed helical pile in sand, 50mm in diameter and with rib length of 8 mm, may be up to 5 times higher than that of a straight plain pile. The authors found that the capacity increase depended on the rib spacing, $s$, and that the maximum capacity occurs at an $s/d$ ratio of approximately 1, where $d$ is the diameter of the pile (without ribs). Similar conclusions were found by Merifield (2011), $s/d$=1.58, and Rao *et al.* (1991), $s/d$ =1.0 - 1.5, studying the uplift capacity of helical anchor plates in clay, where $d$, in this case, is the diameter of the plate. The slight increase in critical spacing is probably due to the different failure mechanism for these anchor plates. Both Gorasia and McNamara (2016) and Qian *et al.* (2016) found that ribbed piles have a higher capacity than straight piles with a diameter equal to the outer diameter of the ribbed pile.

A major issue associated with ribbed piles is the removal of spoil from the bore prior to concreting. To address this, an alternative method of increasing pile/soil interface roughness is to profile the shaft walls by creating small impressions that lead to a nodular pile surface; this avoids the generation of any loose spoil. A special tool has been developed by Keltbray Piling (Patent no: P027299GB/JMF/ZJH) to undertake this profiling, at prototype scale, and create what has been termed an “impression pile”. It is this form of pile shaft friction improvement that is the focus of this research project. A conceptual sketch of the impression pile is shown in Figure 1, together with the ribbed pile reported for comparison purposes. In the simplest configuration, four nodules are impressed at a given cross section, spaced at 90º around the axis of the pile, and nodules are aligned in the vertical direction, although other configurations may be used.
Following the successful proof of concept, (Lalicata *et al.,* 2020), a large parametric study in the geotechnical centrifuge has been carried out to explore the influence of impressions on the ultimate capacity of a pile. The results are described in this paper. A possible failure mechanism is developed to explain the results obtained. The equipment developed for model pile testing was designed to be flexible in order to permit testing of a wide range of possible impression configurations.

## 1. Experimental work

### *1.1. Methodology*

The enhanced ultimate capacity of impression piles subjected to a static vertical force was explored in centrifuge tests undertaken at 50*g* using a homogeneous overconsolidated clay deposit. In each experiment, the impression piles were tested alongside a plain, straight shafted pile to provide a baseline response for comparison purposes.

The Geotechnical Engineering Research Group at City, University of London, makes use of an Acutronic 661 beam centrifuge, described in detail by Schofield and Taylor (1988) and McNamara *et al.* (2009). The package containing the model was installed on the centrifuge once the piles had been bored, impressed and cast and the loading apparatus assembled on the plane strain strongbox. The whole process took approximately 2 hours.

During the centrifuge tests, the water table was maintained at a depth of approximately 10mm below ground level by means of a constant head standpipe connected to the bottom of the model. The top surface was sealed with a sprayed synthetic rubber coating to prevent clay drying during the test, once dried this was only ∼400 μm thick and it is known to not influence soil settlements (Le, 2017). The sample was allowed to come into pore pressure equilibrium and the piles were then loaded until failure at a displacement rate of 1mm/min.

### *1.2. The experimental arrangement*

For each test, the soil sample provided up to four testing sites within the rectangular strongbox, Figure 2. The piles were positioned on the centreline of the model, 100 mm from the sides, which was far enough to minimise boundary effects (Phillips, 1995).

The piles, were spaced 110 mm apart and loaded simultaneously by means of a very stiff beam connected to a lead screw and motor. The apparatus was devised so that it was possible to obtain independent load and settlement data for each pile. Experimental evidence collected over the years suggest that the capacity of a pile is not affected by neighbouring piles when they are spaced more than 2-3.5d (De Mello, 1969; O'Neill *et al.*, 1982; Cooke, 1986; Conte *et al.*, 2003; Mandolini *et al.*, 2005; De Santis and Mandolini, 2006). Therefore, the pile spacing adopted in this study, 6.9d, is sufficient. This necessitated the development of several novel components. These included a loading system and independent measurement of pile displacement together with the guides, jigs and impression tools needed to create the model piles. The details of these are given in Lalicata *et al.* (2020).

### *1.3. "Impression pile"*

The test piles were 16mm in diameter and 180 mm long, replicating a prototype pile 800mm in diameter by 9m long. The pile length to diameter ratio of 11.25 is small if compared to typical piles used in the field, which can be up to 50, but a reasonable compromise given the need to provide sufficient soil under the base of the piles and the limited depth of clay available. The nodules on the model test piles protruded from the shaft by 1.5mm $\pm$0.05mm and were 3mm $\pm$0.05mm wide, as measured post-test. As shown in Figure 3, two different nodule shapes were tested. The first had a circular cross section and a domed head, whilst the second had a square side with a flat pyramidal tip. The shapes had the same maximum protruded length and cross-sectional dimension (diameter = square side = 3mm).

The piles were excavated using a 16mm diameter thin walled stainless-steel tube guided by a collar to guarantee verticality. An innovative impression tool was developed to form the nodules. It was designed to be smaller than the bore diameter when closed and to form the impressions when open, Lalicata *et al.* (2020). For a given depth the tool impressed two nodules at a time, and was then rotated by 90 degrees for the second pair of nodules along an orthogonal axis. A sketch of the vertical cross section of the impression tool and the guide system is shown in Figure 4.

Once the impressions were completed, the piles were cast using a polyurethane fast cast resin, Sika Biresin G27 (McNamara, 2001; McNamara and Taylor, 2002; Gorasia and McNamara, 2016). Aluminium powder was used as filler to increase the weight of the pile. The mixture was designed to have a good fluidity to fill the impressions. The resulting pile density was 1.45 g/cm$^3$, the components placed on the pile head to accommodate the loading and measurement equipment provided an additional dead weight of 13.4N or 21.6N (at 50*g*) depending on the type of instrumentation installed, Lalicata *et. al.* (2020). Uniaxial compression tests were undertaken to measure the mechanical properties of the resin when set. The resin was found to have a Young's Modulus equal to 1.1GPa and a yield stress of 35MPa. These values confirm that the pile behaves as a linear elastic material in the range of the applied loads.

### *1.4. Soil*

The Speswhite Kaolin clay used in the tests was prepared from slurry with an initial water content of approximately 120%; which is twice the liquid limit. The slurry was created by mixing dry powder and distilled water in an industrial ribbon blade mixer.

The slurry was carefully placed into the model container and manually agitated to expel the main air bubbles. The inside faces of the model container had been previously coated with water pump grease to minimise friction at the boundaries (Philipps, 1995). Beneath the slurry there was a filter paper and a 3 mm porous plastic sheet, with an aluminium drainage plate at the base. On top of the slurry, a second filter paper and porous plastic sheet were placed and drainage was allowed through holes in a loading platen. Consolidation was achieved by means of a hydraulic press over a period of 9 days including 1 day of swelling. The samples were compressed to a vertical stress of 500kPa that was then reduced to 250kPa, producing a firm, but still workable, clay sample (McNamara *et al.*, 2009; Taylor *et al.*, 2012; Divall and Goodey, 2015; Gorasia and McNamara, 2016).

Following testing on the centrifuge, the undrained shear strength was estimated from hand vane tests and water content samples. The water content of samples taken from the model, Figure 5 (a), were converted to soil strengths using eq. (1) (Wood, 2004) and values of relevant parameters published by Stallebrass and Taylor (1997) with a small adjustment to the value of the specific volume on the critical state line at a mean effective stress of 1kPa, $\Gamma$. This was changed from 2.997 to 3.04 in order to obtain values of strength consistent with those from the hand shear vane. The values of the parameters and their meaning are listed in Table 1.

$$s_u = \frac{1}{2} M e^{\frac{(\Gamma - v)}{\lambda}} \tag{1}$$

where $v$ is the specific volume.

Soil strength measurements for the tests are given in Figure 5 (b) and (c) respectively for the values derived from water contents $s_{u,w}$ and for those derived from hand vane tests $s_{u,vane}$. The measurements are largely consistent across all tests and, in both cases, the data are generally inside the 10% error band with respect to the best fit line. As might be expected, the undrained strength increased slightly with depth as water content reduced. The manufacturer of the hand vane (Pilcon, 2020) notes that this should be used for generic in-situ indications only, consequently water content measurements were used to give a more precise indication of the variation in undrained strength for the purposes of normalising the data and a best fit to these data is as follows:

$$s_{u,w} = 41.2 + 0.044z \tag{2}$$

where $s_{u,w}$ is expressed in kPa and $z$ in mm.

The profile of the overconsolidation ratio, *OCR*, with depth for the tests is reported in Figure 5 (d).

# 2. Results

## *2.1. Parameters investigated*

The results of the experimental parametric study are presented in this section. The detail of the nodule dimensions and the main features of the impression pile are shown in Figure 1. The parameters varied were:

- The active length, $L_a$: the portion of the pile shaft where the impressions were created;
- The spacing, $s$: the vertical distance between two levels of nodules
- The number of nodules at a given cross section, $n$;
- The position of the centre of the impressed zone relative to the soil surface, $z$.

The length parameters listed above have all been made non-dimensional as listed in Table 2, which also gives the range of values investigated.

## *2.2. Experimental variability*

The behaviour of the piles has been characterised using their load deflection response. The ultimate compressive capacity $Q_u$ is the asymptotic value of the curve after the peak where the shaft and the base resistance may be assumed fully mobilised. In the model tests, the ultimate capacity of the plain piles ranged between 342N and 430N (model scale), Table 3.

The head displacement was not always sufficient to reach a fully flattened plateau; therefore, the ultimate capacity recorded has, in some tests, been estimated, Figure 6. However, because the increase or decrease in capacity post peak does not vary significantly with settlement the maximum uncertainty in these values is 10N. For each test, $\alpha$ was back calculated from $Q_u$ taking into account the dead weight of the pile, assuming the base resistance was fully mobilised and adopting the $s_{u,w}$ distribution measured in the relevant test. Where the values of ultimate load are estimated, the value of $\alpha$ given varies by up to 0.03.

Following Skempton (1951), the base resistance is expressed as:

$$Q_b = A \cdot q_b = \pi \frac{d^2}{4} \cdot \left(N_c \cdot s_{u(base)} + \sigma_v\right) \tag{3}$$

Where $A$ is the cross-sectional area of the pile base, $N_c$ is the bearing factor, taken as equal to 9, (Meyerhof, 1951; Martin and Randolph, 2001; Khatri and Kumar, 2009) related to the soil strength $s_u$ and $\sigma_v = \gamma \cdot L$ which is the overburden pressure at the base of the pile.

The variation in ultimate capacity from 342N to 430N is significant, but well correlated with the undrained shear strength, $s_{u,w}$ evaluated at $z=L/2$=90mm, Figure 7. In the plot, the grey symbols represent the data where the load settlement curve did not reach a constant value and ultimate capacities have been estimated. The theoretical capacity of the pile is calculated as the sum of the load taken in skin friction along the shaft, $Q_s$, and the load provided by the end bearing, $Q_b$, minus the self-weight, $W$:

$$Q_u = Q_b + Q_s - W \tag{4}$$

The $s_u$ distribution adopted is given by Eq. (2) and an adhesion factor, $\alpha$, equal to 0.73. This is the average back calculated value reported in Table 3. A good correspondence between the theoretical ultimate load and the experimental results is apparent considering the variability of $s_{u,w}$ (see Figure 5 (b)).

### *2.3. Ultimate capacity of the impression pile*

The ultimate capacities of the impression piles are listed in Table 4 together with the main parameters describing the patterns of nodules on the pile shafts, such as the shape and the number of nodules, the active length, the spacing and position of the impression zone along the pile. The nodules protruded from the shaft by 1.5mm and were 3mm wide. If there was insufficient settlement for the ultimate load to be reached this has been estimated following the same approach as was used with the plain piles and with the same maximum uncertainty of 10N. Differences in the load settlement response at large displacement, with respect to the plain piles, are reported and discussed in Lalicata *et al.* (2020).

The influence of the impression variables on the ultimate capacity of the piles is plotted in Figures 8-11. In each figure, plot (a) gives the ultimate capacity presented as a function of the physical variable, described in Table 4, while plot (b) gives the increase in capacity plotted against the normalised variable. The increase in capacity is the ratio of the ultimate capacity of the impression pile and the plain pile evaluated for each test. Theoretically, this procedure should account for any small variation in soil properties between the different tests. In practice, marginal differences in the ultimate capacity of both the impression and the plain pile may result in a small, but not negligible variation in the increase in capacity equal to a maximum of $\pm$5%. In all the plots the pyramidal nodules are pictured as open square symbols and the domed nodules are open circles. The grey symbols represent data from the tests where the ultimate capacity was an estimate because there was insufficient settlement to reach this state and the diamonds represent the piles where the spacing of the pyramidal nodules was very high (60mm and 120mm). To allow comparisons to be made, data from the tests in Table 4 have been selected so that only one parameter is changed in each plot while the others are maintained constant.

The influence of the active length $L_a$ is clearly presented in Figure 8 which shows both the ultimate load and the proportional change in capacity increase with $L_a$. Both of the plots indicate that the shape of the nodules, owing to the small dimensions of the impression, only marginally influence the ultimate capacity of the piles. For comparison, the ultimate capacity of a plain pile is presented in Figure 8 (a) showing that, for constant $L_a$, the variability of the impression pile results is similar or lower than that observed for the plain piles and discussed in the previous section. The effectiveness of the nodules increases with $L_a$, and when this is ~0.85$L$, the increase in capacity is approximately 40%.

Figure 9 presents the influence of the spacing, *s*, between nodules. When *s* increases from 30mm to 60mm the ultimate capacity drops significantly (Figure 9 (a)). For $s$<30mm the pile response is similar allowing for experimental variability. This appears to be because the failure surface around the nodules bridges vertically creating a vertical block of soil connecting adjacent nodules with the failure surface on the outside of this block. This is supported by inspection of the exhumed piles at the end of the tests. For high spacing, this does not occur and failure takes place by soil flowing around individual nodules. Qualitatively, the normalised plot in Figure 9 (b) shows the same result although the data could be interpreted to show a higher critical spacing. The average increase in capacity is ~25% for the block case, reducing to 12% for the highest spacing of 120mm.

Ultimate capacity increases with the number of nodules *n*, Figure 10 (a). The increase in capacity, Figure 10 (b), increases linearly with the number of nodules and for n=4, all but one set of data are consistent. Inspection of Figure 11 (a) seems to indicate that the position of the impressions *z* has a minor influence on the pile capacity. In both Figures 10 and 11 there is an increased scatter when the data are presented as increase in capacity, which was not expected as this should remove any variability associated with variations in undrained strength.

## 3. Back Analysis of Impression Pile Ultimate Capacity

The results from the centrifuge tests illustrate the main parameters affecting the ultimate capacity of the impression pile.

- The increase in capacity of the impression pile is approximately constant if the vertical spacing is lower than a threshold value, *s/b* between 20 and 40, Figure 9. It is assumed that within this threshold, no relative displacement occurs between the shaft of the pile and the soil between the nodules and the failure surface is on the outside of the nodules that are connected in the vertical direction, Figure 12. When the vertical spacing increases beyond this threshold value, the nodules behave as individual embedded foundations. As the number of nodules reduces in a given active length, the increase in capacity of the impression pile reduces as well.

- Below the threshold spacing, the increase in capacity appears to be a linear function of the number of nodules in the pile cross section; at least for the range explored (see Figure 10). This suggests that the nodules connect in the vertical direction only; forming independent vertical blocks of similar cross-sectional dimensions. A limiting number of nodules will certainly exist, but the data collected in this study do not allow conclusive statements to be made.
- The increase in capacity of the piles is proportional to the length of pile impressed with nodules if the nodules are less than the critical spacing apart.
- The vertical position of the nodules has little effect on pile capacity for the soil conditions studied, $s_u$ only increasing marginally with depth, and the pile geometry tested.

Given the above, the ultimate capacity of the impression pile is calculated by extending design methods for a plain pile and is illustrated in Figure 12 for the block mechanism. The base capacity $Q_b$ remains the same as the straight pile. The shaft capacity $Q_s$ is divided in two parts: one inside the active length $L_a$, $Q_{s,in\ La}$ and the other outside the active length, $Q_{s,out\ La}$. Inside the active length the shaft resistance develops in a different manner with respect to the nodules, $Q_{s,nod}$, and the pile shaft, $Q_{s,intra\ nod}$. Finally, an additional contribution is provided by the bearing capacity of the nodule $Q_{b,nod}$ that is included only once, for the lowest nodules in the group. For simplicity it is assumed that the failure surface in the horizontal plane has the same cross-sectional dimensions as the nodule.

The base resistance is calculated with eq. (3). Outside the impressed zone the skin friction is the same as the plain pile:

$$Q_{s,out\ L_a} = \pi d \cdot \alpha s_u (L - L_a) \tag{5}$$

Inside the active length the two contributions are:

$$Q_{s,nod} = n \cdot 4b \cdot s_u \cdot L_a \tag{6}$$

$$Q_{s,intra\ nod} = (\pi d - 2b \cdot n) \cdot \alpha s_u \cdot L_a \tag{7}$$

In the block, it is assumed for simplicity that the failure occurs in the soil only, where the adhesion factor is taken as equal to one. Due to the small dimensions of the nodules, eq. (6) neglects the reduction in $\alpha$ at the nodule/soil interface. For constant $\alpha$ values, the accuracy of this assumption increases as the spacing increases. Between two blocks, failure takes place on the shaft of the pile, where $\alpha$ is assumed to be the value back calculated from the plain pile test.

When the spacing between the nodules is higher they behave as individual embedded foundations, such that $L_a$=0 and $Q_{s,nod}$ = $Q_{s,intra\ nod}$ = 0 and $Q_{b,nod}$ must be evaluated for each nodule horizon .

The end bearing of the nodules is:

$$Q_{b,nod} = n \cdot A_{nod}\left(N_{c,nod} s_u + \sigma_v\right) \tag{8}$$

Where $A_{nod}$ is the cross-sectional area of the nodule; equal to $2b^2$ in this case. The bearing factor $N_{c,nod}$ is calculated using an upper bound solution presented in the next section.

*3.1.1.End bearing of the single nodule*

The failure mechanism around a single nodule is three-dimensional, thus 3D conditions should be considered. However, as a first approximation, the end bearing of a nodule can be assumed to be similar to that of a section of a rib and the rib can be studied under axisymmetric conditions. Thus, the spread of the failure mechanism around a single nodule in the horizontal direction is not considered for simplicity and consistency with the lateral extent of the block mechanism described above. The bearing factor for the rib, $N_{c,rib}$, is derived using upper bound theorems of plastic collapse for a rigid perfectly plastic weightless material with a Tresca failure criterion. The adhesion factor on the soil-rib interface, $\alpha$, is varied from 0 (smooth) to 1.0 (rough). The mechanism is similar to that of a deep buried anchor plate (Merifield and Smith, 2010; Merifield, 2011; Martin and Randolph, 2001) although in this case the presence of the pile shaft cannot be neglected.

The assumed failure mechanism and the associated hodograph are presented in Figure 13: below the rib, there is an annular wedge of soil attached to the rib that slides along a surface inclined at 45° to the horizontal. Beside the wedge, a fan zone with internal angle 3/4$\pi$, guarantees kinematic compatibility and finally another block of soil, the same height as the rib, rises as the rib descends.

The expression for the bearing factor of the single rib is thus:

$$N_{c,nod} = N_{c,rib} = \xi\Big((2+3\pi) + \big(\sqrt{2} + \big(2+\sqrt{2}\big)\cdot\alpha\big)\Big) \tag{9}$$

Where $\xi$ is a shape factor accounting for the axisymmetric conditions, it decreases with decreasing *b/d* ratio and is practically independent from $\alpha$. Here $\xi$ is equal to 1.097. Further details on the $N_{c,rib}$ and $\xi$ derivation are given in the Appendix A. $N_{c,rib}$ is equal to 14.11 for $\alpha$=0 and to 17.81 for $\alpha$ =1.

*3.1.2. Critical vertical spacing*

The experimental data showed that the impression piles perform best when the nodules form a block in the vertical direction, when the bearing factor of the single nodule is relatively insignificant in determining the behaviour of the impression pile. Consequently, understanding when the nodules behave as a block or independently in the vertical direction is crucial for the design of the impression pile. The experimental results in Figure 9 suggest that this critical spacing may range between 20*b* and 40*b*. Using the bearing factor in eq. (9) it is possible to express the critical spacing as a function of the geometry of the impression and the pile and of the adhesion factor.
The critical vertical spacing is estimated by comparing the load capacity resulting from two independent ribs and the shaft capacity developed between them; with the load capacity resulting from the block failure connecting the two ribs.
If the circumference of the pile plus rib is $P_{ext} = 2\pi\cdot\left(\frac{d}{2}+b\right)$ and the circumference of the pile is $P_{pile} = \pi d$, the critical vertical spacing when $Q_s$ is equal for both mechanisms, is given by:

$$Q_{s,block} = P_{ext} \cdot \; [s_u \cdot (s - 2b) + \alpha s_u \cdot 2b]$$

$$=$$

$$Q_{s,single} = A_{rib} \cdot N_{c,rib} \cdot s_u \; + P_{pile} \cdot \alpha s_u \cdot 2b \qquad (10)$$

$$\downarrow$$

$$\frac{s}{b} = \frac{1}{\left(P_{ext} - \alpha P_{pile}\right)} \cdot \left[\frac{A_{rib}}{b} N_{c,rib} - 4\alpha \cdot P_{pile} + 2P_{ext}(1 - \alpha)\right]$$

Eq. (10) is presented as a function of $\alpha$ in Figure 14, which shows that the normalised critical spacing, *s/b,* increases sharply from $\alpha$=0.8 to 1. This indicates that when the value of shear strength of the soil-pile interface approaches that of the soil, the block mechanism prevails; whatever spacing is used. Eq. (10) represents an "envelope" above which single nodule behaviour is predicted to dominate and below which the block mechanism is predicted. For $\alpha$ values between 0.6 and 0.8, as in the centrifuge tests, the *s/b* ratio varies from 27.9 to 41.2 which is consistent with the experimental results.

### *3.2. Comparison with experimental data*

In the previous section, the expressions for the bearing factor and the critical vertical spacing of the nodules were derived for the simplified case of axisymmetric conditions (ribbed pile). However, as noted these expressions can also be used to interpret the data from the impression piles. In the series of tests undertaken, a block mechanism in the vertical direction occurs except for T12 where piles were tested with *s/b* equal to 40 and 80. If it is assumed that the nodules do not interact in the horizontal direction, which is consistent with the linear increase in $Q_u$ with number of nodules at a given horizon, the ultimate capacity can be computed by considering the capacity provided by a series of vertical ribs coincident with the nodules as shown in Figure 12. For each prediction, the value of adhesion and the shear strength distribution used to predict the load capacity are those measured in the relevant test.

In Figure 15, the sum of the measured load and the dead weight of the pile is compared with the predicted net load ($Q_s$+$Q_b$), calculated using equations (3) to (8). The comparison shows compatibility between both the block and the independent nodule tests, as all of the predictions lie inside a 10% error band. The predicted capacities tend, on average, to slightly underestimate the measured capacities.

This gives clear evidence that, for the range of geometries tested in overconsolidated clay, the method set out above is an effective means of undertaking a theoretical calculation of the ultimate capacity of an impression pile. It can be demonstrated that, due to the small dimensions of the nodules, the end bearing contribution of the lowermost level of nodules, $Q_{b,nod}$, is very small compared to their contribution in creating the block mechanism . For instance, when $n$=4 it is approximately 3.0% of the total ultimate capacity. Therefore, the use of the simplified axisymmetric analysis for the study of the bearing factor, eq. (9), appears more than justified.

## Conclusions

The paper presents the results of an investigation into the enhanced pile capacity of impressed piles with an improved soil/pile shaft interface created using a method developed by Keltbray Piling. The concept consists of profiling the shaft walls by creating impressions that form nodules projecting into the soil when the pile is concreted leading to an increased soil-pile roughness and moving the failure surface away from the shaft into the soil. An extensive parametric study was carried out in a series of geotechnical centrifuge model experiments. The tests modelled bored piles in overconsolidated clay. In each test the impression piles were tested together with one plain pile against which the impression piles could be assessed.

As with all modelling techniques, centrifuge modelling has some level of idealisation which may not be completely representative of prototype situations. In the tests, installation effects are neglected as the piles were installed at 1*g* rather than in the high-*g* environment. This is clearly not representative of the prototype scale installation but may be considered as an ideal wished in place installation of the pile. The resin used to cast the piles was also an idealisation since the adhesion between the resin and Speswhite kaolin clay sample may not be representative of the adhesion between concrete and a heavily overconsolidated clay. However, both these idealisations lead to results that would be conservative with respect to an equivalent pile in the field, i.e. the beneficial effects of the impression piles would be enhanced as the shaft resistance of the plain concrete piles in the field would be lower owing to the lower soil to pile adhesion relative to the model piles.

The main outcomes of this study may be summarised as follows:

- The increase in capacity of the impression piles depends on the proportion of the pile impressed, which has been termed the active length, $L_a$. When $L_a$~0.85$L$, the increase in capacity reaches 40%. Therefore, an impression pile having the same capacity as the plain pile could be reduced in dimensions by ~37% in length or ~25% in diameter;
- There exists a critical vertical spacing, of between 20*b* and 40*b*, for the nodules at which the failure mechanism of the pile changes. If the spacing is lower than the critical threshold, the failure surface connects the nodules along a vertical alignment. When the vertical spacing is greater than the critical value the failure occurs around each nodule independently of surrounding nodules;
- The relative increase in bearing capacity increases approximately linearly with the number of nodules at a given cross section. This is because, in the range explored, the failure surface around the nodules connects in the vertical direction only and not in the horizontal plane. There will be a limit to the number of nodules for which this is true, however, the data collected do not allow this limit to be clearly defined.

A method for the calculation of the ultimate capacity of the impression pile was established using an upper bound solution under axisymmetric conditions. Although this is technically incorrect, as the nodule failure is three-dimensional, some findings are still valid especially those in the (vertical) plane of the application of the load. The upper bound solution provides an expression for the bearing capacity of the single nodule and an expression for the vertical critical spacing that depends on geometric variables and on $\alpha$. The critical spacing is in good agreement with the experimental results and it is a key element in the design of these foundations.

The calculation method considers explicitly the contribution provided by the shear stress developed along the vertical blocks of soil between the nodules, the skin friction on the remainder of the shaft and the end bearing of the blocks. The predictions are in extremely good agreement with the experimental data with a discrepancy of less than 10%. The calculation method detailed in this paper has been used to define the design method for the impression pile presented in Lalicata *et al.* (2021).

The study has demonstrated the benefit to be gained in pile capacity by profiling the shaft of bored cast in situ piles in clays. The increase in capacity of the impression pile is very promising and the technology used has the potential to minimise uncertainties in shaft capacity for these commonly used piles at prototype scale because the pile capacity relies less on the pile adhesion factor. The analysis method developed explains the main features of the results based on an appreciation of the mechanisms by which the piles fail and will be a useful tool for designers. Further work is currently being undertaken to explore the link between the ultimate capacity of the piles and the performance at working loads.

**Acknowledgements**

This research project would not have been developed without funding from Innovate UK and the vision of Keltbray Piling. They are gratefully acknowledged. The authors also want to thank technical staff from City, University of London for their support in the manufacture of all the components of the experimental set-up. Finally, we would like to thank Professor Neil Taylor and Professor Michael Davies for their suggestions; Dr Richard Goodey, Dr Sam Divall and all the geotechnical research group for sharing knowledge and stimulating discussion.

**References**

Cherubini C. & Vessia G. (2007). Reliability approach for the side resistance of piles by means of the total stress analysis ($\alpha$ method). *Canadian Geotechnical Journal*, **44**, No. 11, 1378–1390.

Conte G., Mandolini A., and Randolph M. F. (2003). Centrifuge modeling to investigate the performance of piled rafts. *Proc. Geotech. Int. Seminar on Deep Foundations on Bored and Auger Piles*, Van Impe and Haegeman, eds., 379–386.

Cooke R.W., Price G. and Tarr K. (1980). Jacked piles in London clay: Interaction and group behaviour under working conditions. *Géotechnique*, **30**, No.2, 97–136.

De Mello V.F.B. (1969). Foundations of buildings on clay. State-of the- Art Report, *Proc. VII ICSMFE*, Vol. **1**, 49–136.

de Sanctis L and Mandolini A. (2006). Bearing capacity of piled rafts on soft clay soils. J*. Geotech Geoenviron Eng.* 132, No. 12, 1600–1610.

Divall S., and Goodey R.J. (2015). Twin-tunnelling induced ground movements in clay. *Proceedings of the Institution of Civil Engineers: Geotechnical Engineering*, **168**, No.3, 247–256.

Gorasia, R. J. & McNamara, A. M. (2016). High-capacity ribbed pile foundations. *Proceedings of the Institution of Civil Engineers: Geotechnical Engineering*, **169**, No. 3, 264–275.

Ground Engineering (2003). Getting to grips with friction. *Ground Engineering, Magazine of the British Geotechnical Association* **26**, 20–21.

Hard D.A. and Carvalho A.T. (2018). Threaded rotary bored piles at Paddington new yard. *Proceeding of the 2018 DFI-EFFC International Conference on Deep Foundations and Ground Improvement*, Rome, Italy.

Karkee M.B., Kanai S. and Horiguchi T., (1998). Quality Assurance in Bored PHC Nodular Piles Through Control of Design Capacity Based on Loading Test Data. *Proceedings of the 7th International Conference and Exhibition*, Piling and Deep Foundations, Vienna, Austria, **1**(24):1-9.

Khatri V. N. and Kumar J. (2009). Bearing capacity factor Nc under φ=0 condition for piles in clays. *Int. J. of Numerical and Analytical Methods in Geomechanics*; **33**, No 9, 1203–1225.

Lalicata L. M., McNamara A. M. and Stallebrass S. E. (2020). Experimental technique for creating enhanced capacity piles in a centrifuge environment. *Proc. of European Conf on Physical Modelling in Geotechnics ECPMG2020, Lulea*, 49-55.

Lalicata, L.M., McNamara, A. M. and Stallebrass, S. E. (2021). Design method for the "impression pile". *Institution of Civil Engineers: Geotechnical Engineering*. https://doi.org/10.1680/jgeen.21.00033.

Lalicata L.M., McNamara A.M., Stallebrass S.E. and Panchal J.P. (2021). Physical Modelling of High-Capacity Piles under Axial Loading. *Proc of the Piling 2020 Conference*. 259-264. ICE Publishing. https://doi.org/10.1680/pttc.65048.259

Mandolini A. (1999). Small-strain soil stiffness and settlement prediction for piled foundations. *Proc. ff the 2nd Int. Symposium on Pre-failure Deformation Characteristics of Geomaterials*, Turin, Italy. 1397–1404.

Mandolini A., Russo G. and Viggiani C. (2005). Piled foundations: Experimental investigations, analysis and design. State-of-the-Art Report. *Proc. of the 16th ICSMGE*, Osaka, Japan, Vol. **1**, 177-213.

Martin C. M. and Randolph M. F. (2001). Applications of the lower and upper bound theorems of plasticity to collapse of circular foundations. *Proc. of 10th Int. Conf. on Computer Methods and Advances in Geomechanics, Cairns*, 2; 1417–1428.

McNamara A.M. (2001). Influence of Heave Reducing Piles on Ground Movements Around Excavations. *PhD thesis*, City University, London, UK.

McNamara A.M. and Taylor R.N. (2002). Use of heave reducing piles to control ground movements around excavations. *Proc. Int. Conf. Physical Modelling in Geotechnics*, St' John's, 847-852. Balkema, Rotterdam

McNamara A.M., Goodey R.J. and Taylor, R.N. (2009). Apparatus for centrifuge modelling of top down basement construction with heave reducing piles. *International Journal of Physical Modelling in Geotechnics*, **9**, No. 1, 1-14. https://doi: 10.1680/ijpmg.2009.9.1.01

Merifield R.S. (2011). Ultimate uplift capacity of multiplate helical type anchors in clay. *J. of Geotechnical and Geoenvironmental Engineering*, **137**, No. 7, 704–716.

Merifield R.S. and C. C. Smith. (2010). The ultimate uplift capacity of multi-plate strip anchors in undrained clay. *Computers and Geotechnics,* **37**, No. 4, 504-514.

Meyerhof G.G. (1951). The ultimate bearing capacity of foundations. *Géotechnique*, **2**, No. 4, 301-332.

O'Neill M.W., Hawkins R. A., and Mahar L. (1982). Load transfer mechanisms in piles and pile groups. *J. Geotech. Engrg. Div.*, **108**, No. 12, 1605–1623.

Phillips R. (1995). Centrifuge modelling: practical Considerations. In *Geotechnical Centrifuge Technology* (Taylor RN (ed.)). Blackie Academic and Professional, Glasgow, UK, ch. **3**, 34–59.

Pilcon (2020). Hand vane tester User guide. See http://www.impact-test.co.uk/docs/SL815_HB.pdf . (accessed 02/09/2020)

Qian J.G., Gao Q., Wang B., Xue J.F., and Huang M.S. (2017): Physical and numerical pull-out modelling of ribbed piles. *Proceedings of the Institution of Civil Engineers: Geotechnical Engineering*, **170**, No. 1, 51–61.

Rao S., Prasad Y. and Shetty M. (1991). The behaviour of model screw piles in cohesive soils. *Soil and Foundations*, **31**, No. 2, 35–50.

Schofield A.N. and Taylor R.N. (1988). Development of standard geotechnical centrifuge operations. *Proc. Centrifuge 88*, *Paris*, 29–32.

Skempton A.W. (1959). Cast-in-situ bored piles in London clay. *Géotechnique*, **9**, No. 4, 153-173.

Stallebrass S.E. and Taylor R.N. (1997). The development and evaluation of a constitutive model for the prediction of ground movements in overconsolidated clay. *Géotechnique*, **47**, No. 2, 235-253.

Stanier SA, Black JA, Hird CC (2014) Modelling helical screw piles in soft clay and design implications. *Proceedings of the Institution of Civil Engineers: Geotechnical Engineering*, **167**, No. 5,447–460.

Taylor R.N., Rose A.V. and Gorasia R.J. (2013). Pile and Pile Group Capacity: Some Findings from Centrifuge Tests. *International Journal of Geo-Engineering*, **5**, No. 2, 5-15.

Watanabe K., Sei H., Nishiyama T and Ishii Y. (2011). Static axial reciprocal load test of cast-in-place nodular concrete pile and nodular diaphragm wall. *Geotechnical engineering journal of the SEAGS & AGSSEA*, **42**, No. 2.

Wood D.M. (2004). Geotechnical modelling. New York: Spon Press.

Zhou J.J., Gong, X.N., Zhang R.H., Hesham El Naggar M. and Wang K.H. (2020). Field behavior of pre-bored grouted planted nodular pile embedded in deep clayey soil. *Acta Geotechnica*, **15**, No. 7, 1847-1857. doi:10.1007/s11440-019-00891-x

## Appendix A

In this section the calculations of the bearing capacity of the rib under plain strain and axisymmetric conditions are presented.

With reference to Figure 13 the components of the internal work are listed in Table 5.

The internal work is then:

$$W_{int} = \left( (3\pi + 2) + \frac{h}{b} \cdot \left( \frac{\sqrt{2}}{2} + \left( \frac{2+\sqrt{2}}{2} \right) \cdot \alpha \right) \right) \cdot \delta \cdot b \cdot s_u \quad (11)$$

As the pile is a rigid body, the external load can be conveniently applied on the rib length *b* instead of the pile head. The external work is thus:

$$W_{ext} = Q_u \cdot \delta = q_u \cdot b \cdot \delta \quad (12)$$

Equating eq. (11) and (12) the bearing factor $N_{c,PL}$ under plane strain conditions is:

$$N_{c,PL} = (3\pi + 2) + \frac{h}{b} \cdot \left( \frac{\sqrt{2}}{2} + \left( \frac{2+\sqrt{2}}{2} \right) \cdot \alpha \right) \quad (13)$$

For vanishing heights of the rib, the solution converges to the deeply buried single anchor mechanism developed by Rowe and reported in Merifield and Smith (2010). For $\alpha$=1, the failure mechanism is similar to the second mechanism proposed the authors.

Under axisymmetric conditions, which apply to a ribbed pile, the surface of revolution around the centre line of the pile must be calculated explicitly. This is done by multiplying the work done on each interface or fan in the failure mechanism, see Table 5, with the corresponding revolution surface:

$$W_{fan1,pile} = W_{fan2,pile} = \delta \cdot b \cdot s_u \cdot \pi \cdot (d + b) \quad (14)$$

$$W_{fan1} = W_{fan2} = \frac{3}{2}\pi \cdot \delta \cdot b \cdot s_u \cdot 2\pi \cdot \left( \frac{d}{2} + b \right) \quad (15)$$

$$W_1 = \left(\left(\frac{2+\sqrt{2}}{2}\right)\cdot \alpha \cdot 2\pi \cdot \left(\frac{d}{2}+b\right) + \frac{\sqrt{2}}{2}\cdot 2\pi\cdot\left(\frac{d}{2}+b+\sqrt{2}b\right)\right)\delta\cdot h\cdot s_u \tag{16}$$

Hence the internal work is:

$$\begin{gathered} W_{int} = W_{fan1,pile} + W_{fan1} + W_2 + W_{fan2} + W_{fan1,pile} = \\ = \delta\cdot b\cdot s_u\cdot\pi\left[2\cdot(d+b) + 2\cdot 3\pi\cdot\left(\frac{d}{2}+b\right)\right. \\ \left. + \frac{h}{b}\left(\sqrt{2}\cdot\left(\frac{d}{2}+b+\sqrt{2}b\right) + \alpha\cdot\left(\frac{2+\sqrt{2}}{2}\right)\cdot\left(\frac{d}{2}+b\right)\right)\right] \end{gathered} \tag{17}$$

And the external work is:

$$W_{ext} = Q_u\cdot\delta = q_u\cdot\pi\cdot\left[\left(\frac{d}{2}+b\right)^2 - \frac{d^2}{4}\right]\cdot\delta = q_u\cdot\pi\cdot[b^2+db]\cdot\delta \tag{18}$$

It is possible to notice that in eq. (17) there is a term that is the bearing factor under plane strain conditions. Equating eq. (17) to (18) and reducing gives:

$$q_u = s_u\cdot\left[N_{c,PL} + \frac{b}{(b+d)}\cdot\left(3\pi + \frac{h}{b}\left(\frac{\sqrt{2}}{2}\cdot\left(1+2\sqrt{2}\right) + \alpha\cdot\left(\frac{2+\sqrt{2}}{2}\right)\right)\right)\right] \tag{19}$$

Then, naming A the term inside the round brackets, one could write:

$$\frac{q_u}{s_u} = N_{c,PL} + \frac{b}{(b+d)}\cdot A = N_{c,PL}\cdot\left(1 + \frac{b}{(b+d)}\cdot\frac{1}{N_{c,PL}}\cdot A\right) \tag{20}$$

In eq. (19) the ratio $\frac{q_u}{s_u}$ is the bearing capacity factor $N_{c,rib}$ while the term inside the brackets is termed ξ and is the shape factor that accounts for the axisymmetric conditions. Finally, eq. (20) assumes the form:

$$\frac{q_u}{s_u} = N_{c,rib} = N_{c,PL} \cdot \xi \quad (21)$$

As shown in Figure 16, $\xi$ decreases with decreasing *b/d* ratios and is practically independent from $\alpha$. For the model pile tested, $\xi$ is equal to 1.097.

Table 1: Mechanical parameters of the Speswhite Kaolin clay.

| Parameter | Value |
|---|---|
| Slope of the critical state line in the q-p' space, *M* | 0.89 |
| Specific volume on the critical state line at p'=1kPa, $\Gamma$ | 3.04 |
| Slope of the normal compression line in the *v-lnp'* space, $\lambda$ | 0.18 |
| Specific gravity, $G_s$ | 2.61 |

Table 2: Summary of the variables investigated.

| **Parameter** | **Value** |
|---|---|
| shape | domed, flat pyramid |
| active length, $L_a/L$ | 0.29, 0.67, 0.83, 0.85 |
| vertical spacing, $s/b$ | 5, 10, 13.3, 20, 40, 80 |
| number of nodules, $n$ | 2, 4, 8 |
| position, $z/L$ | 0.21, 0.5, 0.58, 0.77 |

Table 3: Main parameters of the response of the plain piles.

| Test ID | ultimate capacity, $Q_u$ (N) | dead weight, W (N) | back calculated $\alpha$ |
|---|---|---|---|
| T03 | 350 | 37.82 | 0.73 |
| T04 | 410 | 37.82 | 0.79 |
| T05 | 350* | 37.82 | 0.76 |
| T06 | 350* | 37.82 | 0.76 |
| T08 | 400 | 37.82 | 0.73 |
| T09 | 420* | 37.82 | 0.8 |
| T10 | 430* | 37.82 | 0.78 |
| T12 | 342* | 46.18 | 0.6 |
| T13 | 375* | 46.18 | 0.64 |
| T14 | 375 | 46.18 | 0.67 |

* values of ultimate capacity that have been estimated

Table 4: Main parameters of the response of the impression piles.

| Test ID | shape | active length, $L_a$ (mm) | spacing, $s$ (mm) | number of nodules, $n$ | position, $z$ (mm) | ultimate capacity, $Q_u$ (N) | capacity increase |
|---|---|---|---|---|---|---|---|
| T03 | dome | 152.5 | 7.5 | 4 | 88.75 | 490 | 1.4 |
| T04 | dome | 152.5 | 7.5 | 4 | 88.75 | 555 | 1.35 |
| T03 | pyramid | 152.5 | 7.5 | 4 | 88.75 | 510 | 1.46 |
| T04 | pyramid | 152.5 | 7.5 | 4 | 88.75 | 569 | 1.39 |
| | pyramid | 152.5 | 7.5 | 4 | 88.75 | 570 | 1.39 |
| T05 | pyramid | 152.5 | 7.5 | 4 | 88.75 | 490* | 1.4 |
| | pyramid | 52.5 | 7.5 | 4 | 38.75 | 425* | 1.21 |
| | pyramid | 52.5 | 7.5 | 4 | 88.75 | 410 | 1.17 |
| T06 | pyramid | 52.5 | 7.5 | 4 | 138.75 | 405* | 1.16 |
| | pyramid | 150 | 15 | 4 | 90 | 470* | 1.34 |
| T08 | pyramid | 120 | 15 | 4 | 105 | 490 | 1.23 |
| | pyramid | 120 | 30 | 4 | 105 | 475* | 1.19 |
| | pyramid | 120 | 20 | 4 | 105 | 525 | 1.31 |
| T09 | pyramid | 120 | 30 | 4 | 105 | 518* | 1.23 |
| | pyramid | 120 | 20 | 4 | 105 | 515 | 1.23 |
| | pyramid | 120 | 15 | 4 | 105 | 500 | 1.19 |
| T10 | pyramid | 120 | 20 | 4 | 105 | 550* | 1.28 |
| T12 | pyramid | 120 | 60 | 4 | 105 | 410* | 1.2 |
| | pyramid | 120 | 120 | 4 | 105 | 386* | 1.13 |
| T13 | pyramid | 52.5 | 7.5 | 4 | 38.75 | 390* | 1.04 |
| | pyramid | 52.5 | 7.5 | 8 | 38.75 | 450 | 1.2 |
| | pyramid | 52.5 | 7.5 | 2 | 38.75 | 387* | 1.03 |
| T14 | pyramid | 52.5 | 7.5 | 4 | 38.75 | 410 | 1.09 |
| | pyramid | 52.5 | 7.5 | 4 | 38.75 | 390 | 1.04 |

*values of ultimate capacity that have been estimated

Table 5: Calculation of the internal work on the ribs under plain strain conditions.

| Component | Length | Displacement | Strength | Work |
|---|---|---|---|---|
| fan1,P | $\sqrt{2} \cdot b$ | $\frac{\sqrt{2}}{2} \cdot \delta$ | $s_u$ | $b \cdot \delta \cdot s_u$ |
| fan1 | $\frac{3}{4}\pi \cdot \sqrt{2} \cdot b$ | $\frac{\sqrt{2}}{2} \cdot \delta$ | $s_u$ | $2 \cdot \left(\frac{3}{4}\pi \cdot b \cdot \delta \cdot s_u\right)^*$ |
| 1,O | $h$ | $\frac{\sqrt{2}}{2} \cdot \delta$ | $s_u$ | $\frac{\sqrt{2}}{2} \cdot h \cdot \delta \cdot s_u$ |
| 1,P | $h$ | $\left(1 + \frac{\sqrt{2}}{2}\right) \cdot \delta$ | $\alpha \cdot s_u$ | $\left(\frac{2 + \sqrt{2}}{2}\right) \cdot h \cdot \delta \cdot \alpha \cdot s_u$ |
| fan2 | $\frac{3}{4}\pi \cdot \sqrt{2} \cdot b$ | $\frac{\sqrt{2}}{2} \cdot \delta$ | $s_u$ | $2 \cdot \left(\frac{3}{4}\pi \cdot b \cdot \delta \cdot s_u\right)^*$ |
| fan2,P | $\sqrt{2} \cdot b$ | $\frac{\sqrt{2}}{2} \cdot \delta$ | $s_u$ | $b \cdot \delta \cdot s_u$ |

*note that the work made by the fan is 2 times the work made by the circular sector.

**Figure Captions**

Figure 1: Ribbed and impression pile concept.

Figure 2. Model geometry.

Figure 3: Shape of the nodules.

Figure 4: Vertical cross section of the impression tool.

Figure 5: Distribution with depth of (a) water content, (b) shear strength from water content, (c) shear strength form hand vane and (d) OCR at the end of the tests.

Figure 6: Load settlement curves for the plain piles.

Figure 7: Correlation between the ultimate capacity of the plain piles and average values of su evaluated from water content.

Figure 8: Influence of impression parameters on the ultimate capacity: (a) active length La, (b) normalised variables.

Figure 9: Influence of impression parameters on the ultimate capacity: (a) spacing s, (b) normalised variables.

Figure 10: Influence of impression parameters on the ultimate capacity: (a) number of nodules n, (b) normalised variables.

Figure 11: Influence of impression parameters on the ultimate capacity: (a) position along the pile z, (b) normalised variables.

Figure 12: Capacity of the impression pile.

Figure 13: Failure mechanism of the single rib.

Figure 14: Normalised critical spacing.

Figure 15: Comparison between measured and calculated ultimate capacity of the impression piles.

Figure 16: Shape factor for the rib failure mechanism.

691 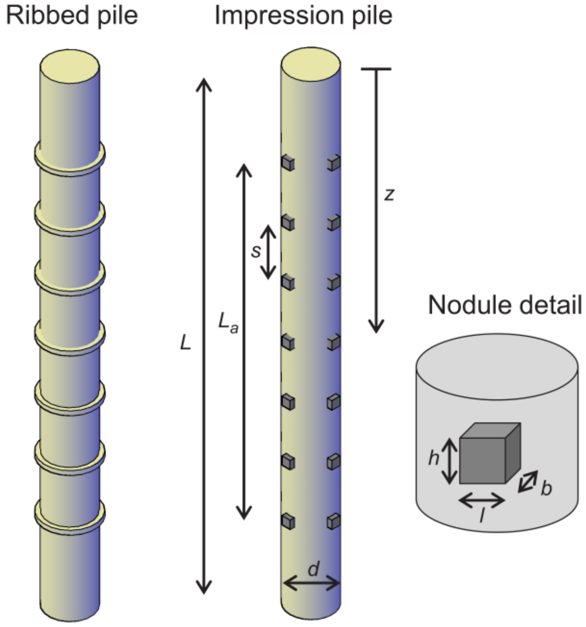

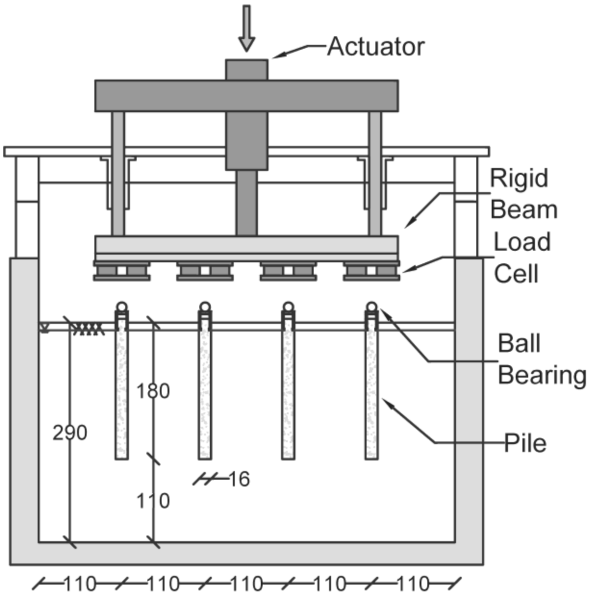
Actuator
Rigid Beam
Load Cell
Ball Bearing
Pile
180
290
16
110
110
110
110
110
110

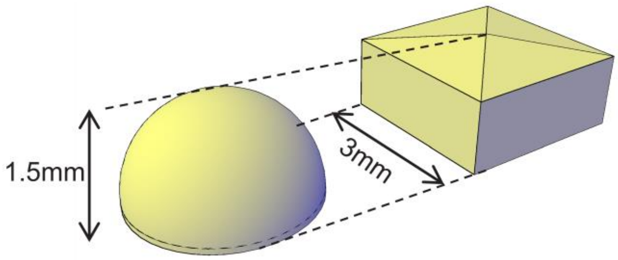
1.5mm
3mm

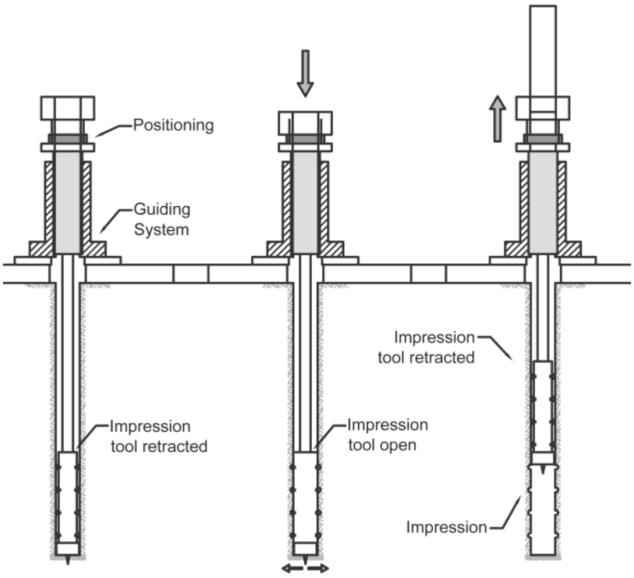
Positioning
Guiding
System
Impression
tool retracted
Impression
tool open
Impression
tool retracted
Impression
694

695

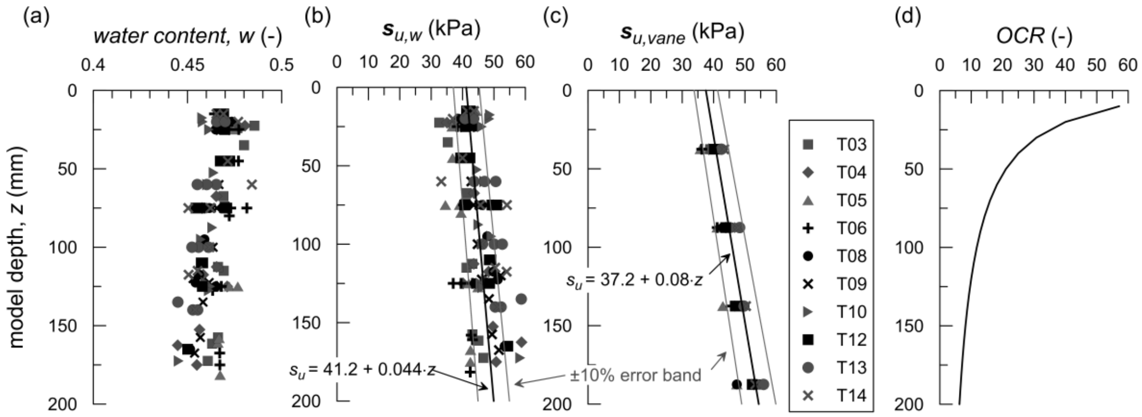

(a)
water content, w (-)
0.4
0.45
0.5
model depth, z (mm)
0
50
100
150
200
(b)
su,w (kPa)
0 10 20 30 40 50 60
su = 41.2 + 0.044·z
±10% error band
(c)
su,vane (kPa)
0 10 20 30 40 50 60
su = 37.2 + 0.08·z
T03
T04
T05
T06
T08
T09
T10
T12
T13
T14
(d)
OCR (-)
0 10 20 30 40 50 60

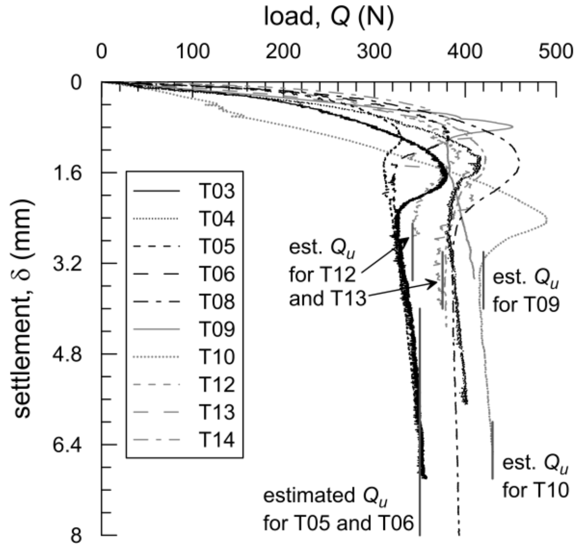
load, Q (N)
0
100
200
300
400
500
0
1.6
3.2
4.8
6.4
8
settlement, δ (mm)
T03
T04
T05
T06
T08
T09
T10
T12
T13
T14
est. $Q_u$ for T12 and T13
est. $Q_u$ for T09
est. $Q_u$ for T10
estimated $Q_u$ for T05 and T06

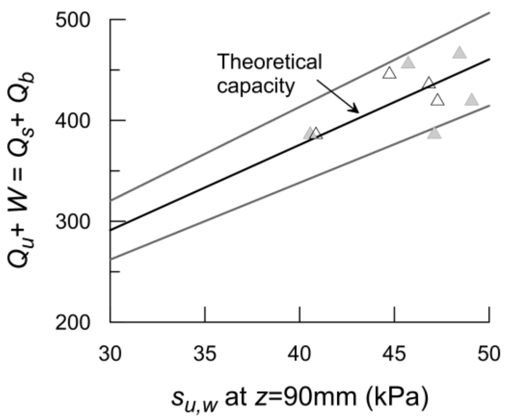
500
400
300
200
30
35
40
45
50
Theoretical capacity
$Q_u + W = Q_s + Q_b$
$s_{u,w}$ at $z$=90mm (kPa)

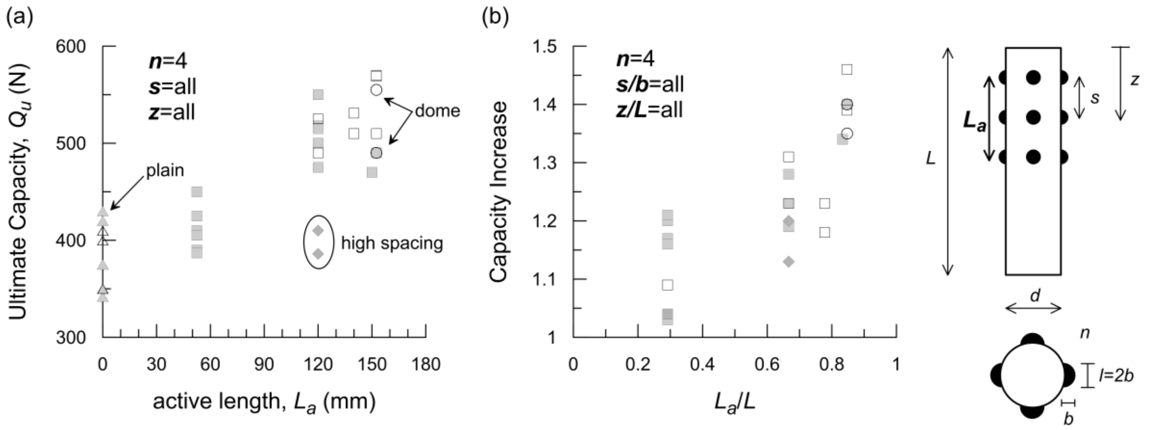
(a)
n=4
s=all
z=all
plain
dome
high spacing
Ultimate Capacity, Qu (N)
active length, La (mm)
(b)
n=4
s/b=all
z/L=all
Capacity Increase
La/L
La
L
s
z
d
n
l=2b
b

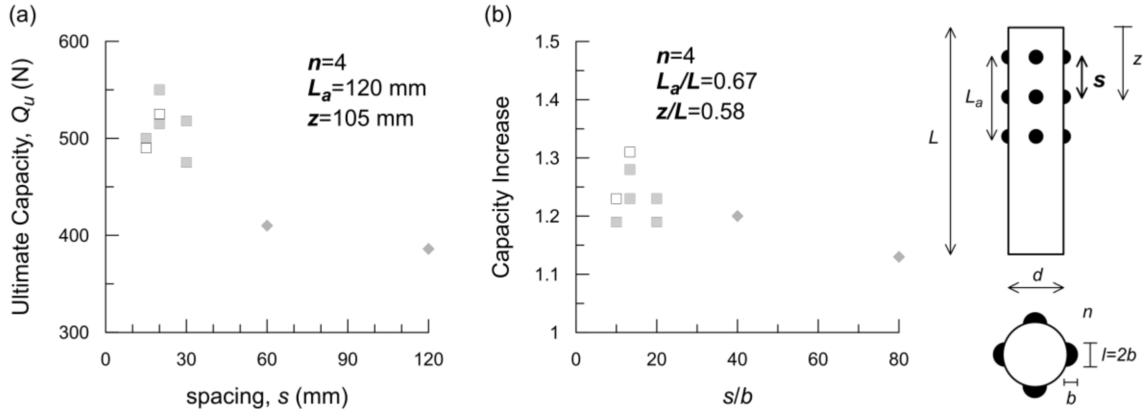
(a)
Ultimate Capacity, $Q_u$ (N)
spacing, $s$ (mm)
$\boldsymbol{n}$=4
$\boldsymbol{L_a}$=120 mm
$\boldsymbol{z}$=105 mm
(b)
Capacity Increase
$s/b$
$\boldsymbol{n}$=4
$\boldsymbol{L_a/L}$=0.67
$\boldsymbol{z/L}$=0.58
$L$
$L_a$
$z$
$\boldsymbol{s}$
$d$
$n$
$l$=2$b$
$b$

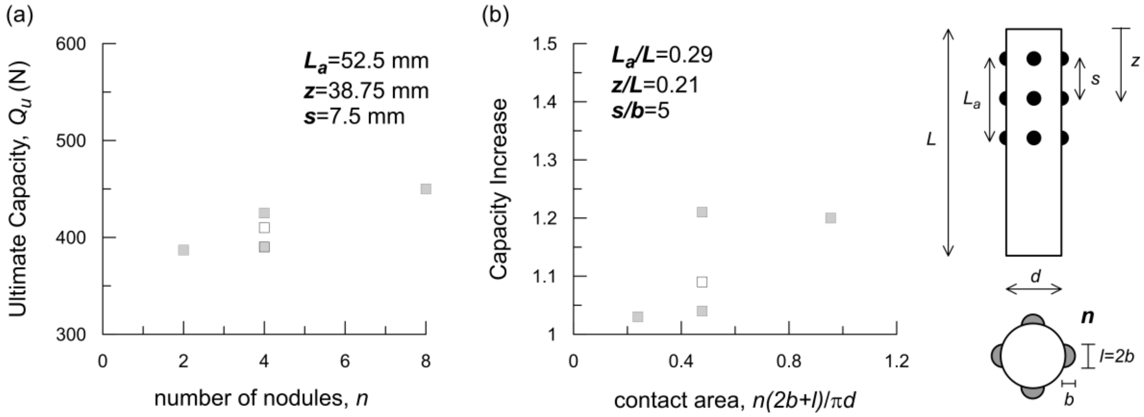
(a)
Ultimate Capacity, $Q_u$ (N)
number of nodules, $n$
$L_a$=52.5 mm
$z$=38.75 mm
$s$=7.5 mm
(b)
Capacity Increase
contact area, $n(2b+l)/\pi d$
$L_a/L$=0.29
$z/L$=0.21
$s/b$=5
$L$
$L_a$
$s$
$z$
$d$
$n$
$l$=2$b$
$b$

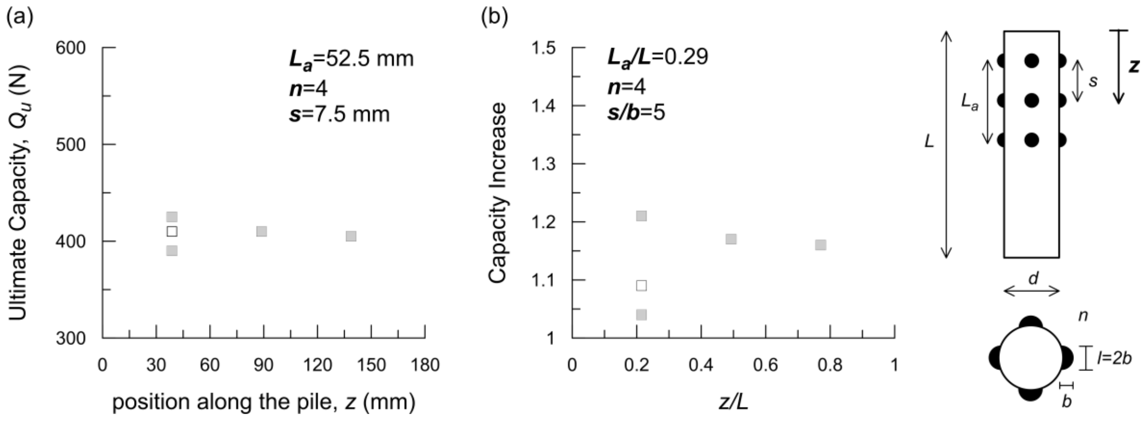

(a)
$L_a$=52.5 mm
$n$=4
$s$=7.5 mm
Ultimate Capacity, $Q_u$ (N)
position along the pile, $z$ (mm)
(b)
$L_a/L$=0.29
$n$=4
$s/b$=5
Capacity Increase
$z/L$
$L$
$L_a$
$s$
$z$
$d$
$n$
$l$=2$b$
$b$

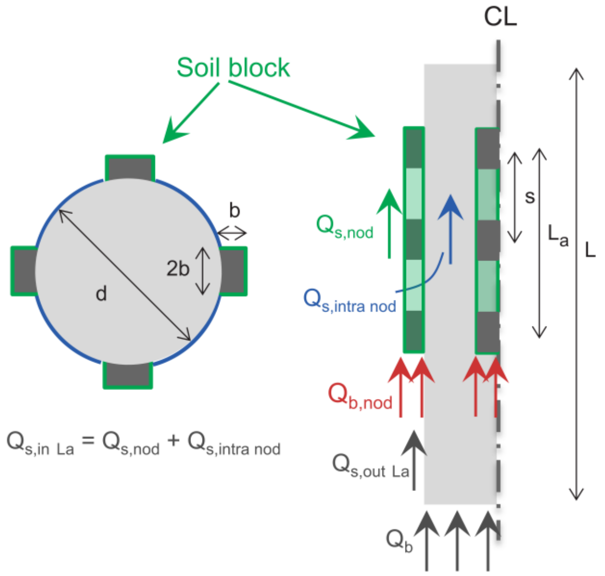

CL
Soil block
b
2b
d
$Q_{s,in\ La} = Q_{s,nod} + Q_{s,intra\ nod}$
$Q_{s,nod}$
$Q_{s,intra\ nod}$
$Q_{b,nod}$
$Q_{s,out\ La}$
$Q_b$
s
$L_a$
L


702

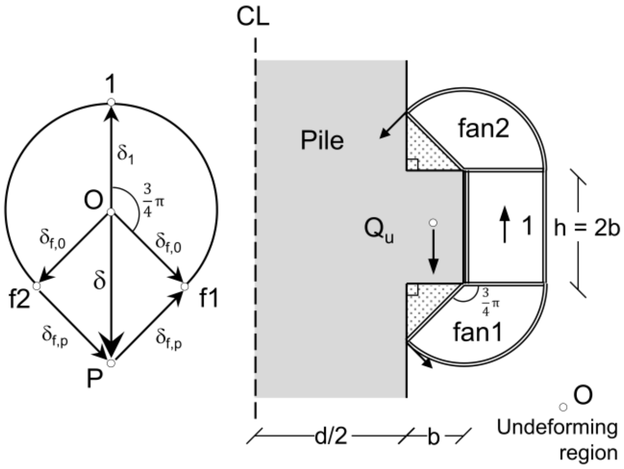

CL
1
$\delta_1$
O
$\frac{3}{4}\pi$
$\delta_{f,0}$
$\delta_{f,0}$
$\delta$
f2
f1
$\delta_{f,p}$
$\delta_{f,p}$
P
Pile
fan2
$Q_u$
1
h = 2b
$\frac{3}{4}\pi$
fan1
O
Undeforming region
d/2
b


703

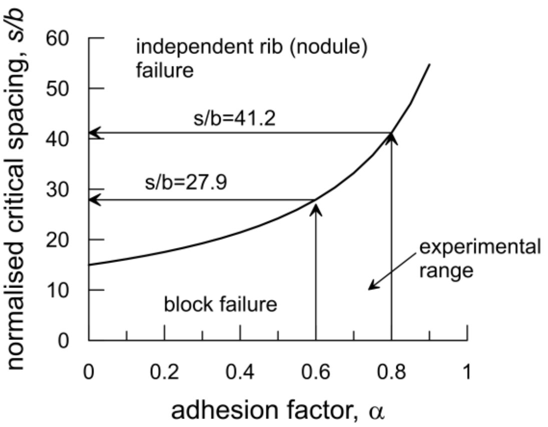
normalised critical spacing, s/b
60
50
40
30
20
10
0
independent rib (nodule)
failure
s/b=41.2
s/b=27.9
experimental
range
block failure
0
0.2
0.4
0.6
0.8
1
adhesion factor, α

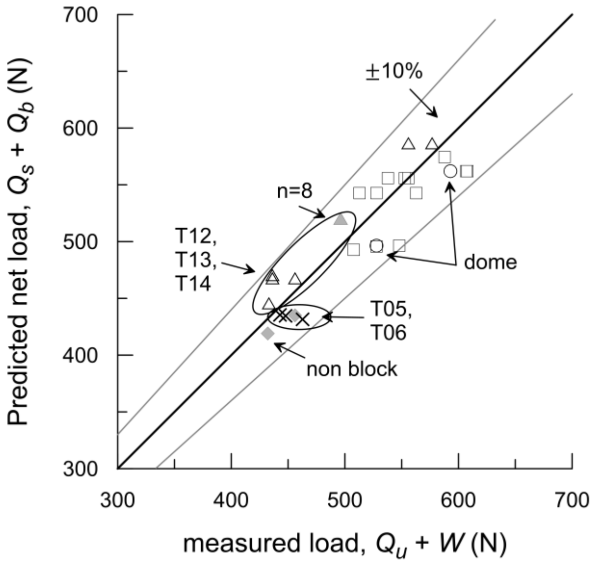
700
600
500
400
300
Predicted net load, $Q_s + Q_b$ (N)
300
400
500
600
700
measured load, $Q_u + W$ (N)
±10%
n=8
T12,
T13,
T14
dome
T05,
T06
non block

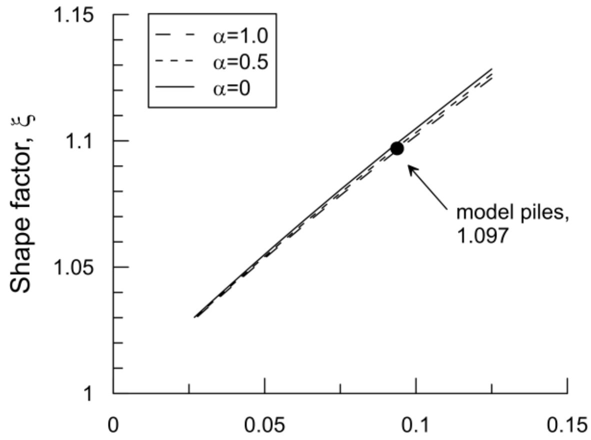

rib to diameter ratio, *b/d*